Contribution of high-temperature 3D-Digital Image Correlation to investigate the creep behaviour of refractory materials

Gilles Dusserre, Thomas Pottier, Thierry Cutard

▶ **To cite this version:**

Gilles Dusserre, Thomas Pottier, Thierry Cutard. Contribution of high-temperature 3D-Digital Image Correlation to investigate the creep behaviour of refractory materials. Open Ceramics, 2023, 15, pp.100425. 10.1016/j.oceram.2023.100425 . hal-04192708

HAL Id: hal-04192708

https://imt-mines-albi.hal.science/hal-04192708

Submitted on 31 Aug 2023

HAL is a multi-disciplinary open access archive for the deposit and dissemination of scientific research documents, whether they are published or not. The documents may come from teaching and research institutions in France or abroad, or from public or private research centers.

L'archive ouverte pluridisciplinaire **HAL**, est destinée au dépôt et à la diffusion de documents scientifiques de niveau recherche, publiés ou non, émanant des établissements d'enseignement et de recherche français ou étrangers, des laboratoires publics ou privés.

Distributed under a Creative Commons Attribution - NonCommercial - NoDerivatives 4.0 International License

Open Ceramics 15 (2023) 100425

Contents lists available at ScienceDirect

Open Ceramics

journal homepage: www.sciencedirect.com/journal/open-ceramics

Contribution of high-temperature 3D-Digital Image Correlation to investigate the creep behaviour of refractory materials

Gilles Dusserre *, Thomas Pottier, Thierry Cutard

Institut Clément Ader (ICA), Université de Toulouse, CNRS, IMT Mines Albi, INSA, ISAE-SUPAERO, UPS, Campus Jarlard, F-81013, Albi, France

ARTICLE INFO

Handling Editor: P Colombo

Keywords:
Refractory
Creep
High-temperature
3D-Digital Image Correlation
Numerical simulation
Drucker-Prager

ABSTRACT

Potential contributions of 3D-Digital Image Correlation are investigated to understand the dilatant behaviour of a refractory concrete during high-temperature creep experiments. An experimental analysis of high-temperature image quality is performed. The measurement uncertainty is assessed and compared to the sensitivity of computed kinematic fields to the parameters of the Drucker-Prager model that control the dilatancy. Promising results are found i) concerning deflection and neutral axis location measurement in bending creep tests and ii) contactless measurement of axial strain in compression creep tests, iii) to support the assumption of dilatant behaviour from bending and diametral compression tests and iv) to provide data for a rough parameter identification from compression creep tests.

1. Introduction

Characterizing the creep behaviour of refractory materials at high temperature remains a complex task due to many experimental difficulties. The materials are intrinsically heterogeneous and achieving the repeatability of high temperature tests is complex, resulting in a variability of the test results. Strain levels of refractories are low and require accurate strain measurements. Furthermore, high temperature creep tests are time and energy consuming and require to learn as much as possible from each test.

In particular, refractories are known to have an asymmetric creep behaviour [1,2], i.e. their creep rate is higher in tension than in compression. This requires to perform mechanical tests under various loading conditions to identify a large number of parameters in modelling approaches. A usual method involves direct tension and compression creep tests [1–3]. This method allows a proper characterization of the behaviour thanks to the uniform stress field applied, and direct identification of unidirectional creep laws. However, the experiments are not straightforward since they require very tedious alignment of the fixtures [4]. Moreover, they are not sufficient to validate the creep models under complex loadings.

In order to provide a complementary insight on the creep behaviour, many authors [5–10] performed bending creep tests. In such experiments, the neutral axis of strain and stress fields shifts toward the initially compressed area due to asymmetric behaviour [11]. This phenomenon is likely to provide a direct information on the asymmetry itself [12–14]. Teixeira [10] proposed to perform diametral compression, i.e. so-called Brazilian tests, in order to apply higher tension stress levels than in bending experiments. Indeed, the centre of the sample is subjected to a triaxial stress state with a positive maximum principal stress. This test can be seen as a complementary test to enlarge the identification creep test database with different stress states, as well as the compressive-shear tests reported in Ref. [15] that are useful to explore different compression-shear ratios.

Digital Image Correlation (DIC) is a powerful technique to perform full-field kinematic measurements. It has been successfully used in many kinds of experiments. Specifically, some authors have reported its use to monitor the strain field in bending creep experiment of ceramics at high temperature [9,10], providing an in-depth characterization of the creep behaviour. This kind of experimental data are very useful to compare simulation results to experimental ones and assess the relevance of models and assumptions [7,9,10,16]. However, its applicability at high temperature is not straightforward because of well-known experimental difficulties [16].

First, heat haze implies a deformation of the sample on the image due to convection inside the furnace, a phenomenon that changes the local refractive index of air between the sample and the camera [17]. In the case of slow rate experiments, as for creep tests, Leplay [9] proposed to have a long exposure time in order to average the effect of this random and high frequency phenomenon. This was achieved thanks to a neutral

* Corresponding author. IMT Mines Albi, Institut Clément Ader, Campus Jarlard – route de Teillet, 81013, Albi, CT cedex 9, France.
E-mail address: gilles.dusserre@mines-albi.fr (G. Dusserre).

https://doi.org/10.1016/j.oceram.2023.100425
Received 3 June 2023; Received in revised form 21 July 2023; Accepted 27 July 2023
Available online 28 July 2023
2666-5395/© 2023 The Authors. Published by Elsevier Ltd on behalf of European Ceramic Society. This is an open access article under the CC BY-NC-ND license (http://creativecommons.org/licenses/by-nc-nd/4.0/).

density filter to avoid saturation.

Second, the availability of a speckle pattern that remains stable at high temperature is another issue [18], which is particularly important for long-time experiments, such as creep tests.

Last, the ratio of reflected to emitted light significantly decreases at high temperature and it requires to carefully choose the image acquisition conditions. For instance, Leplay [9] used powerful white lights in order to have significant reflected light. Pan [19] used blue light and a blue filter to acquire images unsensitive to emitted light.

Among the models available to account for the creep asymmetry, Drucker-Prager creep model (cf. section 2.2.1) has been used in previous papers [16,20] to successfully reproduce the compressive and bending behaviour of a refractory concrete under monotonic loads. The identification was performed under the assumption of associated flow and the curvature of compression sample allowed to evidence a dilatant behaviour. However, the hyperbolic pseudo-potential available in the Abaqus software involves two parameters whose effects have not been thoroughly investigated. First, the dilation angle seems to be close to the friction angle, but effect of small variation in the vicinity of the friction angle is unknown. Second, the eccentricity plays a role mainly in tension and its effect on the neutral-axis location has not been investigated yet. Indeed, eccentricity controls the amount of spherical strain by defining the shape of the hyperbolic pseudo-potential at low Mises equivalent stress. At a given equivalent creep stress, there will be more spherical strain in uniaxial tension than in uniaxial compression. Before handling non-monotonic loadings, a better understanding of these parameters is required. It is noteworthy that the Drucker-Prager creep model is not of general purpose and may not be able to reproduce very high asymmetry, as reported in Ref. [21] for instance.

If the friction angle is not the only parameter that controls the neutral-axis location, as previously assumed, it is mandatory to have available some more information to discriminate the effects of friction angle, dilation angle and eccentricity. Dilation angle and eccentricity do not affect the magnitude of the strain increment, but control the direction of the strain increment (volumetric to deviatoric ratio), mainly for respectively high and low pressures. Investigating the dilatant behaviour in-situ under several loading conditions is expected to provide data to properly identify these parameters.

If monitoring the neutral-axis location in creep bending experiments only requires 2D-DIC, 3D-DIC would give access to out-of-plane displacement [22,23], which is mainly controlled by Poisson effect and dilation. In order to state the benefit of 3D-DIC to the identification of Drucker-Prager creep model parameters, the aim of the paper is twofold. On the one hand, the order of magnitude of out-of-plane displacements as a function of dilation angle and eccentricity will be numerically investigated in axial compression, bending and diametral compression. On the other hand, the level of uncertainty of out-of-plane displacement measurement using 3D-DIC will be assessed.

In a previous paper [8], the natural texture of a refractory concrete surface was used to performed 3D-DIC at room temperature, providing the neutral axis location after interrupted creep bending tests. In the present study, the suitability of the natural texture for 3D-DIC will be assessed at high temperature, on the same material. The experimental investigation is led using the existing furnace, which is equipped with two windows, making it possible to acquire images from two points of view for 3D-DIC, but not allowing the use of additional light.

2. Material and methods

2.1. Material

The material under investigation is a commercial ultra-low cement bauxite-based refractory concrete, reinforced with 2 wt% of FeCrAl hooked-end fibres. Detailed information about the material composition and processing route can be found in previous papers [8,24,25]. The experimental work in the present paper was performed on the bending parallelepipedal specimen labelled *Specimen 10* in Ref. [8] (160 × 39×34 mm^3), and on the cylindrical sample subjected to 3 MPa compression creep for 25 h at 1200 °C in Ref. [20] (height 40 mm and diameter 25 mm).

2.2. Modelling

2.2.1. Constitutive equations

The constitutive law investigated in this study is the Drucker-Prager creep model with an isotropic strain hardening, as available in Abaqus [26]. The creep strain rate, $\dot{\bar{\varepsilon}}^{cr}$, is a function of an equivalent stress $\bar{\sigma}^{cr}$ (Eq. (1)), defined as a function of both Mises equivalent stress, q, and pressure, p, by introducing the so-called friction angle, β (Eq. (2) since the model is calibrated from compression experiment data).

$$\dot{\bar{\varepsilon}}^{cr} = \left[A\left(\bar{\sigma}^{cr}\right)^{n}\left[(m+1)\bar{\varepsilon}^{cr}\right]^{m}\right]^{\frac{1}{m+1}} \tag{1}$$

$$\bar{\sigma}^{cr} = \frac{q - p\tan\beta}{1 - \frac{1}{3}\tan\beta} \tag{2}$$

$$G^{cr} = \sqrt{\left(\varepsilon \bullet \bar{\sigma}_0 \bullet \tan\psi\right)^2 + q^2} - p\tan\psi \tag{3}$$

The computation of the creep strain increment involves a pseudo-potential, G^{cr} (Eq. (3)), function of the dilation angle ψ, Mises equivalent stress q, pressure p, eccentricity ε and the initial yield stress $\bar{\sigma}_0$, used as a homogenization parameter. $\bar{\sigma}_0$ is arbitrarily set to 10 MPa to prevent enabling plastic flow, and the product $\varepsilon \bullet \bar{\sigma}_0$ will be considered as the eccentricity parameter.

2.2.2. Calibration method

The calibration method is briefly described in this section, cf. [16,20] for further details.

The first step of the method uses a set of creep compression test results under several stresses to identify the values of m and n.

$\varepsilon \bullet \bar{\sigma}_0 = 10^{-5}$ is a default assumption providing a quasi-linear pseudo-potential except at the very vicinity of $q = 0$. The hypothesis of normality ($\beta = \psi$) was confirmed *a posteriori* from sample profile curvature [19], allowing the identification of β and ψ from neutral axis location in a bending creep experiment. But experimental evidences are searched to increase the level of confidence.

Finally, A is calibrated by fitting the simulations of compression creep with the experiments. The values reported in Table 1 are those available in Refs. [16,20] and have been identified using plane strain bending computations. They will be used as reference in the present paper to discuss about the out-of-plane displacement.

2.3. Simulation of mechanical tests

This section describes the input data of the simulations of the bending tests used for identification. The axisymmetric simulation of compression tests is detailed in Ref. [20]. As a complement, diametral compression tests were simulated to assess the benefit of such tests for identification of creep laws parameters.

2.3.1. Bending creep tests simulation

The bending creep experiments are usually simulated assuming plane strains [10,20]. In this paper, a focus on the out-of-plane displacements requires resorting 3D solid elements. The reference experiment, already analysed in Refs. [8,16,20] involves a 160 × 39×34 mm^3

Table 1
Parameters of the constitutive law reported in [16,20].

A	m	n	β	ψ	$\varepsilon \bullet \bar{\sigma}_0$
$MPa^{-n} \bullet s^{-(m+1)}$	–	–	°	°	MPa
$3.54 \bullet 10^{-5}$	− 0.593	0.716	42.9	42.9	10^{-5}

parallelepipedal specimen subjected to four-point bending (lower span $L = 125$ mm and upper span $l = 45$ mm) under 400 N for 25 min at 1200 °C.

Considering the symmetries of the problem, a quarter of the specimen is included in the simulation. The part is meshed with 27776 linear hexahedral elements C3D8 (of edge 1.25 mm). A 5 mm wide and 2.5 mm deep partition has been defined to apply an elastic behaviour in both specimen-roller contact areas, Fig. 1.a.

The support and loading rollers are modelled by discrete rigid surfaces meshed with 1368 linear quadrilateral elements R3D4 (of edge 0.5 mm). A friction coefficient of 0.6 was assumed between the concrete and the alumina rollers, cf. [16].

The proper boundary conditions are applied to account for the symmetries. The reference point of the lower roller is fixed. All degree of freedom of the reference point of the upper load are fixed, except the displacement in the y-direction. Before enabling creep behaviour, a small y-displacement of 2 μm is applied on the upper reference point in a first step in order to initiate contact algorithm, and a 100 N concentrated force is then applied in the y-direction instead of the displacement. The creep behaviour is activated in a third step, still applying the force for 25 min.

2.3.2. Diametral compression creep test simulation

Bending creep test is a way to apply tensile load on the material more easily than through direct tension. As an alternative, Teixeira [10] proposed to perform diametral compression tests in order to be able to apply higher tensile stress levels.

For the discussion about the out-of-plane displacement from numerical tests, simulation of Brazilian test in the same configuration as reported by Teixeira [10] are included in the numerical database, with the same material assumptions as previously presented. For the purpose of the discussion, solid elements are used instead of plane strain elements. The specimen is a 50 mm diameter cylinder of length 40 mm, subjected to 800 N load applied on two diametrically opposed generative lines of the cylinder by concavely curved tools of radius 32.5 mm, Fig. 1.b.

One eighth of the sample is included in the simulation, considering 3 symmetry planes. The part is meshed with 7840 linear hexahedral elements C3D8. The loading tool is modelled as a discrete rigid part meshed with 600 linear quadrilateral elements R3D4. A friction coefficient of 0.6 was considered at the contact between the concrete and the tool, cf. [16].

Symmetry planes are applied to model the whole specimen properly and all the degrees of freedom of the reference point that controls the tool are fixed, except the vertical y-displacement. Before enabling creep behaviour, a small y-displacement of 2 μm is applied on the reference point in a first step in order to initiate contact algorithm. A 200 N concentrated force is then applied in the y-direction instead of the displacement. The creep behaviour is activated in a third step, still applying the force for 1 h.

2.4. High temperature 3D DIC

In this section, a set of preliminary results is reported in order to assess the feasibility of 3D-DIC measurement at 1200 °C in the resistive furnace available (cf. Fig. 2.c of reference [27] for an overview). The three main issues for DIC at high temperature are the heat haze, the speckle pattern persistence and the emission of red and near infra-red light. After a presentation of the equipment used, a characterisation of the heat haze is presented. The stability of the natural texture is not problematic here, but the quality of the pattern for DIC is discussed. The furnace used is equipped with two windows, allowing to acquire images from two points of view for 3D-DIC, but without additional light. Therefore, a high amount of emitted light is unavoidable. A specific focus is made on the spectral composition of the images.

2.4.1. Optical equipment

Two 8-bits monochrome CCD digital cameras (Pike® Allied Vision F-505B, 2452 pixels × 2054 pixels, pitch 3.45 μm) are used. The vergence angle between the focal axis of the cameras was 60°, as imposed by the furnace construction. The quantum efficiency of the sensor is plotted in Fig. 2.a according to the curve available from 400 to 1000 nm in the manufacturer datasheet [28]. These data have been extrapolated considering the data of Pike® F-210B between 300 and 400 nm and Pike® F-1100B camera between 1000 and 1100 nm.

Each camera was equipped with an aspherical lens (Tamron 28–200 mm f/3.8-f/22 XR Di). The transmission spectrum of the lenses has been measured using an optical setup comprised of a halogen lamp, a tube lens (FL 20 mm), the lens to be characterized, an integrating sphere and a spectrometer (Ocean Optics USB-650 RedTide Spectrometer from 350 to 650 nm, Ocean Optics USB2000+ Spectrometer from 650 to 1100 nm). The transmission spectrum (Fig. 2.b) is the ratio of spectra obtained with and without placing the lens to be characterized in the optical path.

For comparison purpose, Fig. 2.c reports the spectra available in Refs. [29–32] and shows that most photographic lenses are very similar.

The resistive furnace used to heat the specimen is equipped with two circular glass windows of diameter 50 mm with an angle of 60°. The transmission spectrum of the windows was measured using an IRTF spectrometer (Bruker® Vertex 70) equipped with a Si photodiode to enable measurement in both visible and VSWIR (Very Short-Wave InfraRed) spectral bands. These results show that the transmission at room temperature is almost constant between 450 and 2500 nm and the assumption of constant transmission on the camera sensitivity range (300–1100 nm) will be assumed. The mean value between 450 and 1100 nm is 0.92, cf. Fig. 3.a.

Coloured glass filters (green, blue and red) were used in some

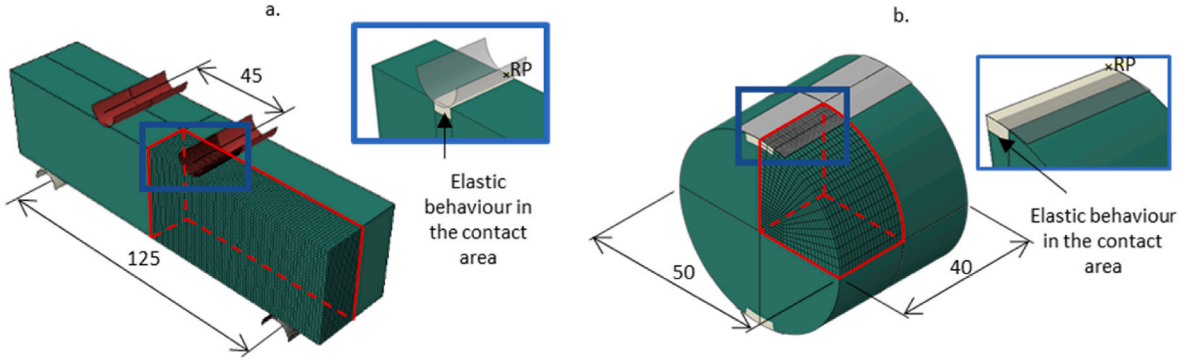

Fig. 1. Description of the simulation of (a.) the bending and (b.) the diametral compression tests. Only the meshed areas are included in the simulations. Symmetry planes are outlined in red. Dimensions in mm. RP: Reference Point. (For interpretation of the references to colour in this figure legend, the reader is referred to the Web version of this article.)

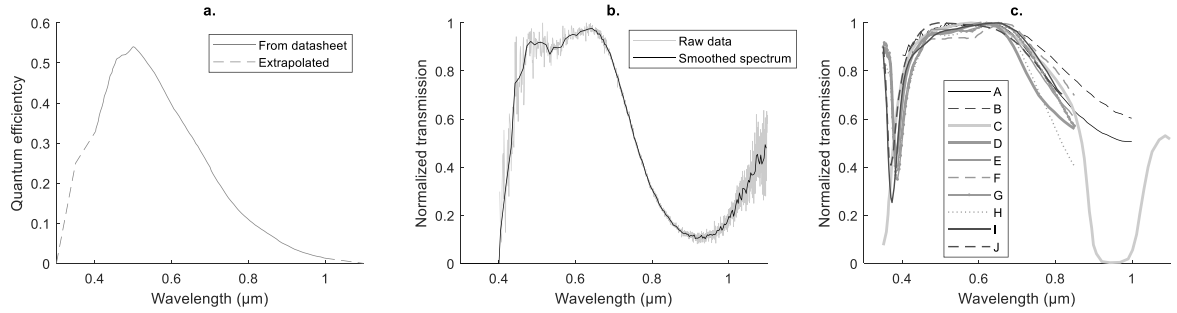

Fig. 2. (a.) Quantum efficiency of the CCD cameras Pike® Allied Vision F-505B [28], (b.) normalized transmission spectra of the lenses used in this study (Tamron 28–200 mm f/3.8-f/22 XR Di) and (c.) normalized transmission of several lenses (A: Canon EF 50 mm f/1.4 USM [29], B: Nikon 50 mm f/1.4 AF-D [29], C: Nikon 55 mm [32], D: Tamron 15–35 VC [30], E: Tamron 85 mm f/1.8 VC [30], F: Nikon 16-35 mm f/4 G [30], G: Nikon 70-200 mm f/4 G [30], H: Nikon 24-85 mm f/3.5-f/4.5 G [30], I: Canon 24 mm f/2.8 IS [31] and J: Canon 28 mm f/1.8 [31]).

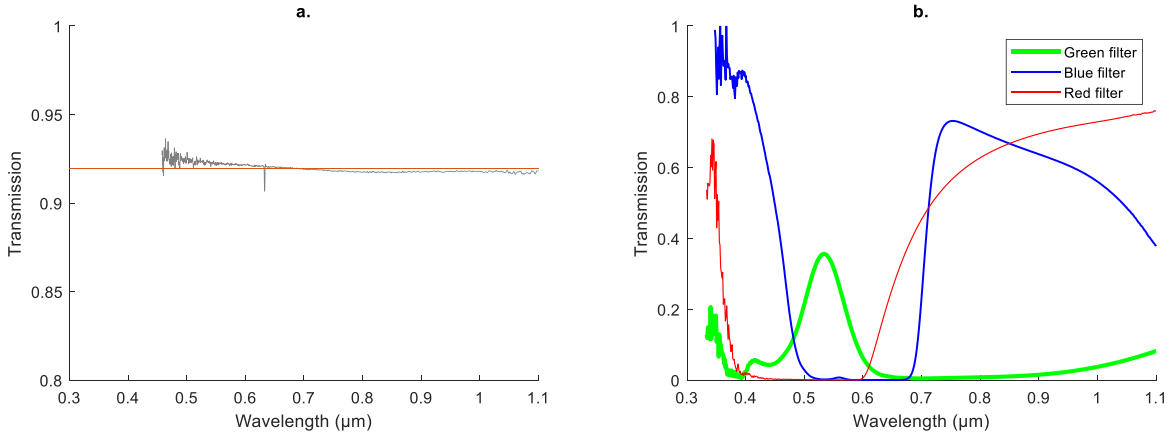

Fig. 3. (a.) Transmission spectrum at room temperature of the furnace glass windows and (b.) transmission spectrum at room temperature of the green, blue and red filters. (For interpretation of the references to colour in this figure legend, the reader is referred to the Web version of this article.)

experiments and their transmission spectra were measured using the same method as the windows spectrum (Fig. 3.b).

In Fig. 4 are plotted the spectral composition of the images assuming white light and black body emission at 900, 1000, 1100 and 1200 °C, by convoluting the camera quantum efficiency, the lens transmission and

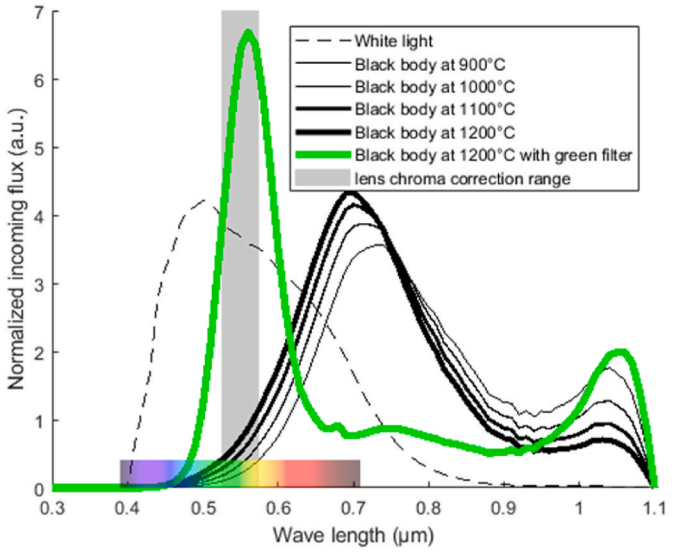

Fig. 4. Normalized spectra of incoming flux toward the sensor for several assumptions (white light and black body emission at different temperatures).

eventually the green filter. The window transmission is independent on wavelength in the range of interest and was thus not considered. Each spectrum was normalized according to the integrated intensity in order to achieve similar grey level, what is done by tuning the integration time in the experiments.

The expected effect of the green filter is to improve the contrast thanks to the high sensitivity of the incoming flux to changes in wavelength. Indeed, a slight difference in wavelength between the light emitted by two constituents will result in a large difference in grey level, thus increasing contrast. Moreover, the incoming flux mainly spreads in the range of lens chroma correction, which is expected to improve the sharpness.

2.4.2. *Characteristics of the heat haze effect*

A set of 100 images of a fixed sample were snapped with the stereo-rig at 5 Hz without any filter and with the green filter. The typical physical size of a pixel is 0.018 mm. 2D-DIC was performed using VIC-2D on subsets of 29 pixels × 29 pixels with a step of 7 pixels, taking the first image as reference, in order to assess the level of displacement related to heat haze. Fig. 5 shows the typical histogram for one image of horizontal and vertical displacements without any filter and with the green filter. It is noteworthy that the left and right images without any filter were acquired synchronously.

Fig. 6 displays the average displacements for each image as a function of time for 20 s (100 images), together with the standard deviation and 95th and 99th percentiles, d_{95} and d_{99}, such that respectively 95 and 99% of the measures are lower than d_{95} and d_{99} in absolute value. The results are overall similar and stable, but right images sequences exhibit

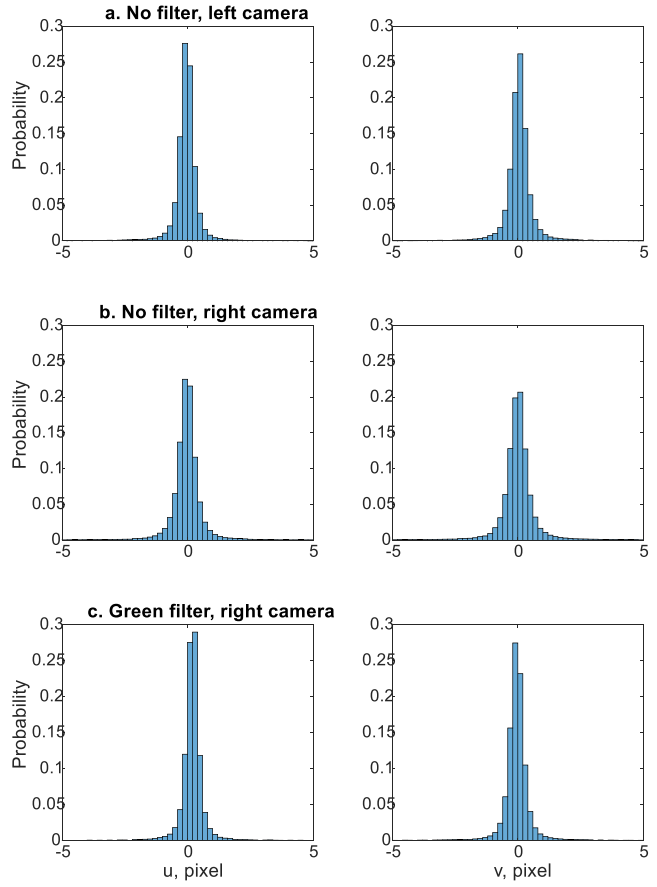

Fig. 5. Typical horizontal (u) and vertical (v) displacements histogram (a.) without any filter, left camera (integration time 1.4 ms), (b.) without any filter, right camera (integration time 1.4 ms) and (c.) with the green filter, right camera (integration time 68 ms). (For interpretation of the references to colour in this figure legend, the reader is referred to the Web version of this article.)

some short instability periods of a few second, either with or without the green filter. The optical path related to the right camera is next to the door of the furnace. The right images are therefore more likely affected by air motion and disturbances along the optical path.

However, the maximum value of d_{99} is 3.5 pixels (63 μm). The overall results over the 100 images are reported in Table 2 and show that 99% of the displacement measurements are below 3.3 pixels (59 μm). For right camera images, data for the first 10 seconds, without perturbation, are reported, too.

According to the results in Table 2, the green filter has not a significant effect on the results. The displacements seem barely less dispersed despite a much longer integration time, and a slight bias (0.14 pixels, i.e. 2.5 μm) is evidenced on the vertical displacement, with a slow shift of the average value (Fig. 6.c left).

As a result, heat haze can be an issue for measurement of low displacement, but its effect in unperturbed periods is as low as 1 pixel (18 μm) for 95 % of the measurements with very small subsets of 0.52 mm (29 pixels). The biggest issue is that left and right images are affected differently by heat haze, with a risk of biasing stereo-correlation. Very long integration time of a few tens of seconds, as proposed in Ref. [9], is a way to overcome this issue by averaging the heat haze effect.

2.4.3. Effect of temperature on image quality

To assess the effect of temperature, a set of ten images was acquired at 1000, 1100 and 1200 °C without filters and averaged. The integration time was set to 9, 4 and 1.4 ms respectively in order to obtain raw images with similar grey levels. The characteristics of the mean images were compared in terms of grey level histograms and Mean Intensity Gradient (MIG, Eq. (4)), with m and n respectively the width and height of the area of interest (AOI) in pixel, and $f_x(\boldsymbol{x_{kl}})$ and $f_y(\boldsymbol{x_{kl}})$ the grey level gradient at pixel $\boldsymbol{x_{kl}}$ respectively in x-direction and y-direction), which is an indicator of speckle pattern quality for DIC [33]. It is noteworthy that the raw images have a higher MIG (typically between 10 and 15) than the mean images, due to noise and vibrations.

$$MIG = \frac{1}{m \bullet n} \sum_{k=1}^{m} \sum_{l=1}^{n} \sqrt{f_x(\boldsymbol{x_{kl}})^2 + f_y(\boldsymbol{x_{kl}})^2} \tag{4}$$

Histograms in Fig. 7 show a decrease of image contrast as the sample heats up. Indeed, in opaque materials the emissivity is the complementary part of the reflectivity and accordingly when the amount of reflection and emission tends to equalize (as the temperature increases) each material point tends to appear equally grey thus resulting in less contrasted images.

The measurement error stemming from such a predictable loss of contrast is well documented and can be partially addressed through the use of ZNCC correlation criterion [33] and contrast adjustment. However, variations of the ratio between speckle size and pixel size (i.e. a decrease in image sharpness) is known to impair drastically the convergence of the DIC algorithms. Indeed, two phenomena can be responsible for a loss of sharpness: i) the presence of convective cells along the optical path (especially if unventilated) [34] and ii) chromatism arising from the spectral shift of the incoming flux away from the centre of the correction wavelength (around 550 nm).

Quantifying the image sharpness can be performed through the computation of the Modulation Transfer Function (MTF), defined as a function of the spatial frequency f in pixel^{-1}, Eq. (5), where $L(\boldsymbol{x_{kl}})$ is the grey level of pixel $\boldsymbol{x_{kl}}$. m and n are respectively the number of columns and lines of the AOI. The sample surface is of course not a sharpness calibration target and thus do not exhibit a constant spatial frequency content. However, comparing the MTF at different temperature of the same surface allows to compare the ability of the imaging apparatus to capture high frequency feature (thus allowing either to improve DIC convergence or to decrease the subset size).

$$MTF(f) = \sum_{k=1}^{m} \sum_{l=1}^{n} L(\boldsymbol{x_{kl}}) e^{-2i\pi f \frac{l-1}{n}} \tag{5}$$

Fig. 8 displays the MTF of images at room temperature with additional light and without additional light from 615 up to 1200 °C, after histograms adaptation (using contrast-limited adaptive histogram equalization [35]). Similar grey levels on the raw images were achieved by tuning integration time. It is shown in Fig. 8.a that the amplitude decreases at high frequency for all images, but it overall decreases faster at high temperature. For instance, the frequency at MTF = 50% only slightly decreases up to 1150 °C (Fig. 8.b), but the frequency at MTF = 0.5% already drastically decreases between room temperature and 615 °C (Fig. 8.c). Between 1150 and 1200 °C, the MTF drops more steeply irrespective of the frequency. It is thus observed from Fig. 8, that, as the samples are heated up, the spatial frequency content of the images decreases. In other word, images become more blurry and spatial features such as speckled aggregates exhibit smoother edges.

It is also observed that adding a green filter slightly improves the MTF of the image at 1200 °C at high frequency. Up to 0.045 pixel^{-1} (MTF = 10 %), the filter has no significant effect, but at higher frequency, the filter allows to improve the sharpness up to levels obtained at 800 °C at a frequency of 0.16 pixel^{-1} (Fig. 8.a and 8.c). In other words, at 1200 °C, the green filter doesn't improve the ability to account for pattern details bigger than 22 pixels, but allows accounting for pattern details of about 6 pixels as well than without filter at 800 °C. Using the green filter will help decreasing the subset size (about 10 pixels) and give an access to some more detailed information.

This latter observation tends to point the responsibility of chromatic

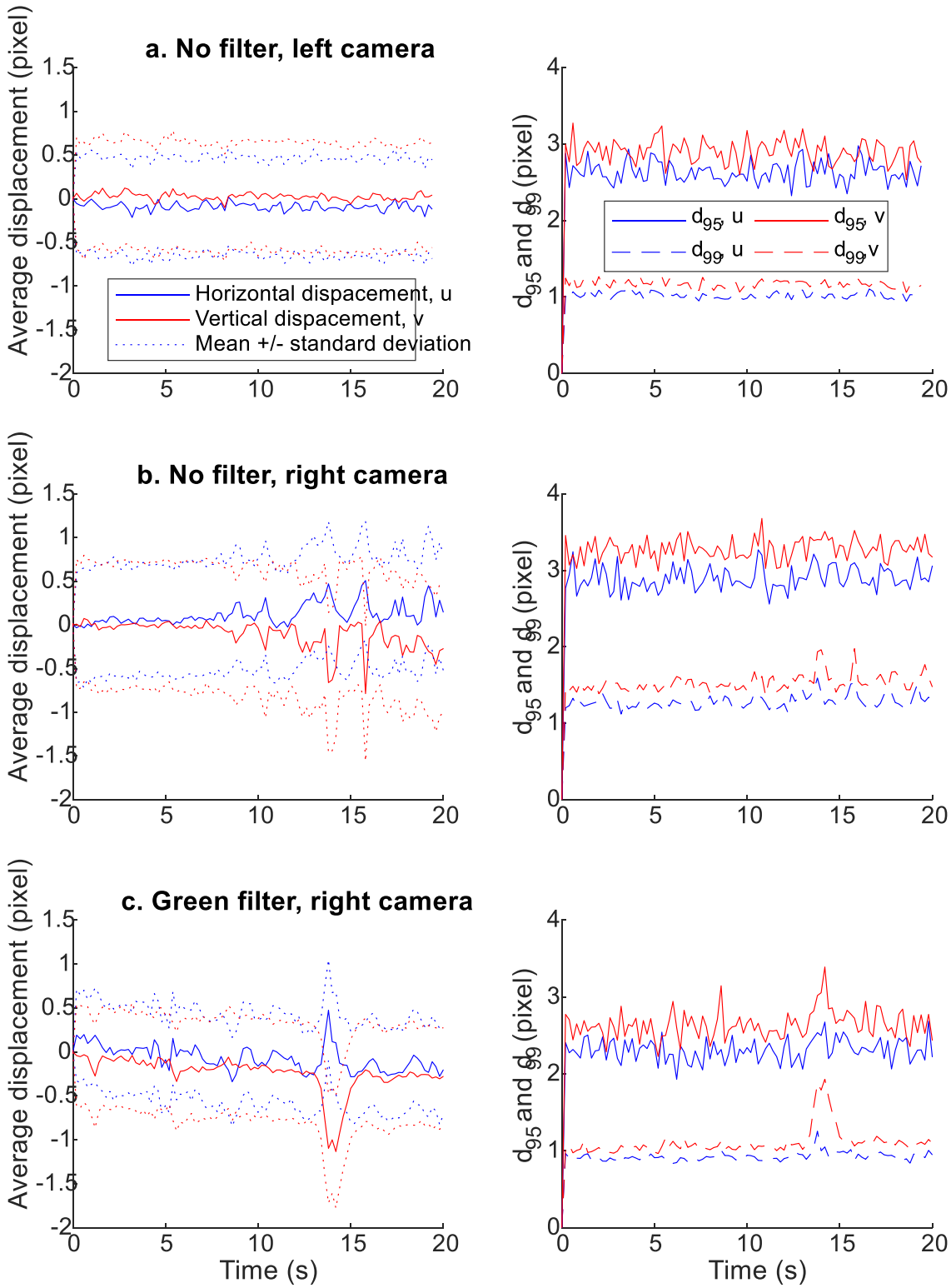

Fig. 6. Average displacement as a function of time (left), and 95th and 99th percentiles, d_{95} and d_{99} (right); without any filter (integration time 1.4 ms) (a. and b.), with green filter (integration time 68 ms) (c.), left camera (a.) and right camera (b. and c.). (For interpretation of the references to colour in this figure legend, the reader is referred to the Web version of this article.)

shift for the loss of sharpness at high temperature. Indeed, as mentioned in the above, at such temperature, the image is composed from reflected illumination light over the sample surface and (in a significant amount) the thermal emission of the sample within the visible spectrum. Although the reflected part of the incoming flux is centred around 550 nm (where the lens is fairly achromatic), the emitted part is mainly located at the right end of the visible spectrum (i.e. red and near-infrared regions, cf. Fig. 4) where the chromatism correction becomes more

Table 2
Statistics of the horizontal (u) and vertical (v) displacements in pixel over 100 images without any filter and with the green filter.

			Average (pixel)	St. dev. (pixel)	d_{95} (pixel)	d_{99} (pixel)
20 s	No filter	u	-0.0906	0.559	1.01	2.61
	Left cam	v	0.0243	0.619	1.16	2.88
	No filter	u	0.122	0.644	1.27	2.87
	Right cam	v	-0.103	0.734	1.51	3.25
	Green filter	u	-0.0759	0.509	0.918	2.29
	Right cam	v	-0.243	0.567	1.10	2.61
First 10 s	No filter	u	0.0663	0.635	1.23	2.82
	Right cam	v	-0.0204	0.721	1.45	3.19
	Green filter	u	-0.0147	0.502	0.890	2.24
	Right cam	v	-0.136	0.561	1.02	2.56

dubious. Using the proposed green filter lead to cut off the incoming flux at such wavelength which in turn tempers chromatic aberrations and improve image sharpness even at a cost of a high integration time (which here again prove some relative insensitivity of the imaging device to the convective motion of the air).

In order to support this conclusion, MTF of images taken at 1200 °C with a blue or a red filter (cf. Fig. 3.b), are plotted in Fig. 8. Using either of these filters allows cutting off the incoming flux in the green range, i.e. in the chroma correction range. Transmission in the near infrared range is high, allowing a low integration time of 3 ms, much lower than with the green filter (68 ms), which is favourable to higher sharpness. However, Fig. 8 shows that the MTF of the images taken with these filters is lower for frequencies above 0.01 pixel^{-1}, i.e. pattern details of about 100 pixels. As a result, limiting the chromatism by using a filter consistent with the correction range, results in a higher sharpness that allows to better account for small details of the pattern, lower than 20 pixels. This can help to improve correlation convergence or decrease the subset size.

3. Results

3.1. Numerical simulations

3.1.1. Compression creep

Two kinds of data are analysed related to compression creep tests. First, the overall strain as a function of time allows identifying the strain hardening parameters m and n (Eq. (1)). Secondly, the sample profile is expected to be sensitive to dilation angle and eccentricity.

Fig. 9. shows the compression creep strain computed with several values of dilation angle and eccentricity. These results show that the compression creep strain curve is almost insensitive to these parameters. Indeed, after 25 h creep at 1200 °C under 3 MPa, all the curves remain within a strain range of 10^{-3}. The order of magnitude of the strain achieved after 25 h is 1.5 %.

Figs. 9 and 10 show that compression creep tests are unsensitive to eccentricity up to $\varepsilon \bullet \overline{\sigma}_0 = 10^{-1}$ MPa. Increasing this parameter up to 2 MPa has a slight effect on the strain (Fig. 9), and a noticeable effect on the sample profile (Fig. 10). For low eccentricity up to $\varepsilon \bullet \overline{\sigma}_0 = 10^{-1}$,

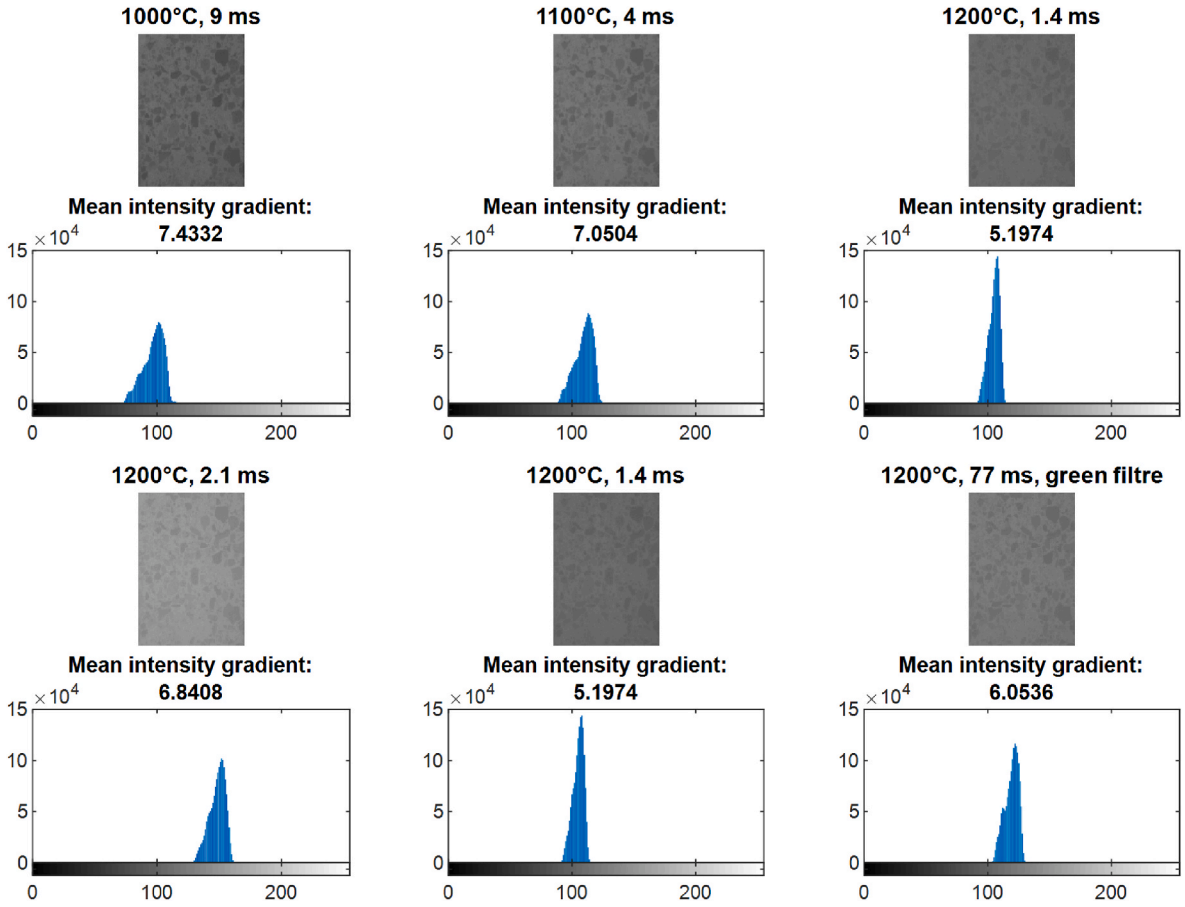

Fig. 7. Effect of temperature, integration time and green filter on MIG of mean images. (For interpretation of the references to colour in this figure legend, the reader is referred to the Web version of this article.)

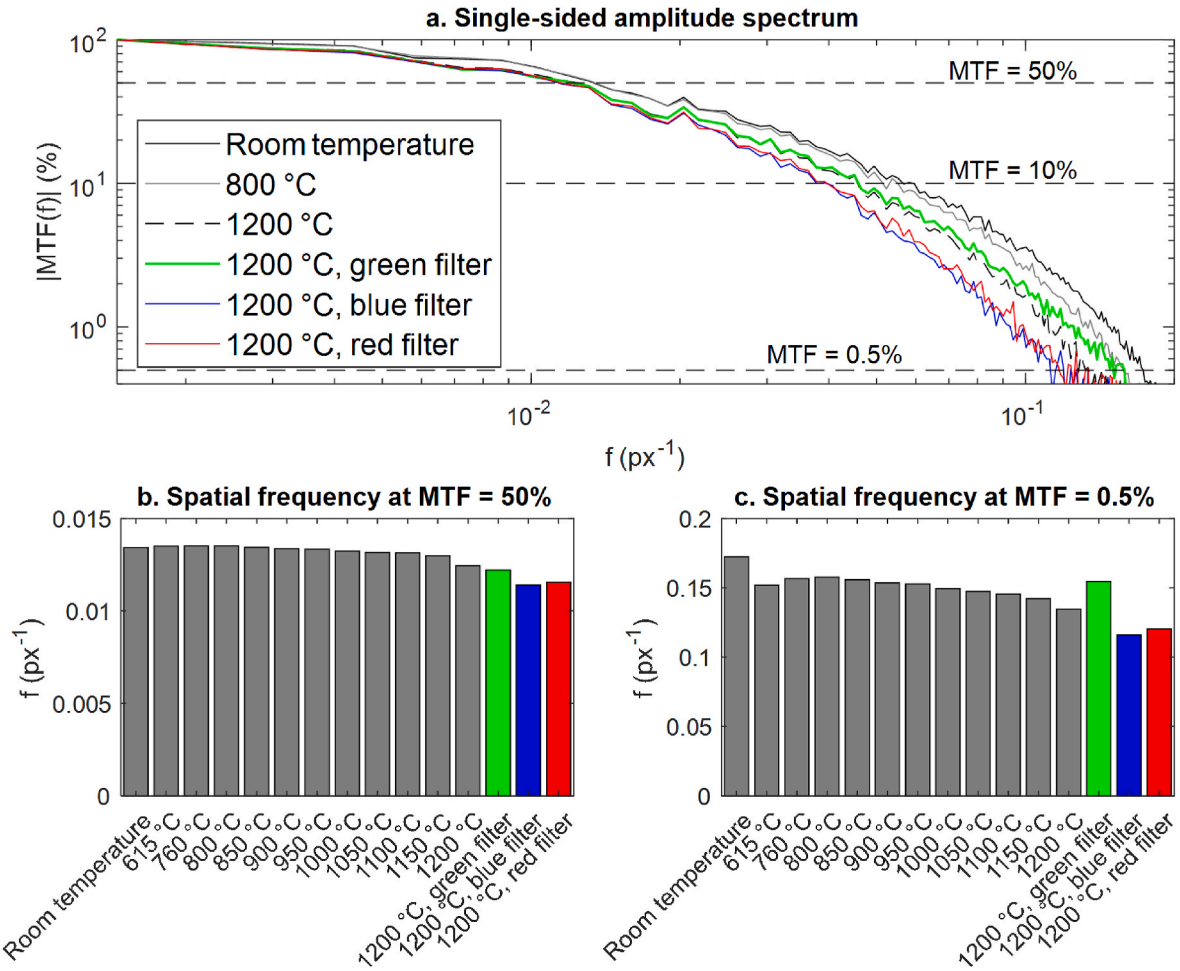

Fig. 8. Single sided amplitude spectrum (a.) and spatial frequency at 50 % (b.) and 0.5 % (c.) amplitude as a function of temperature without filter, and with a green, blue or red filter at 1200 °C. (For interpretation of the references to colour in this figure legend, the reader is referred to the Web version of this article.)

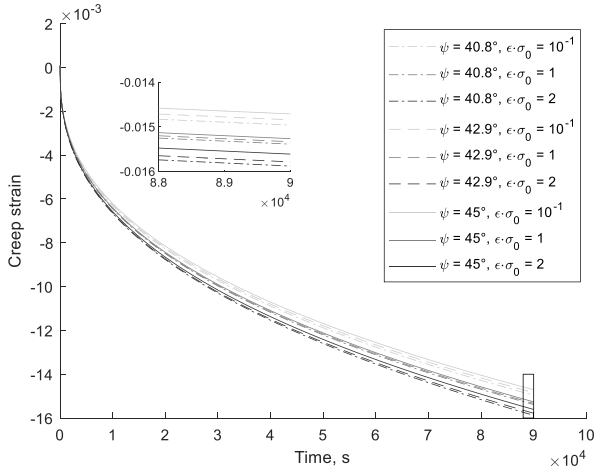

Fig. 9. Creep deformation during compression test at 1200 °C computed with different values of dilation angle, ψ and eccentricity $\varepsilon \bullet \overline{\sigma}_0$ (in MPa).

dilation angle is the only parameter that affects the sample profile, whereas both parameters control the profile for high eccentricity values.

3.1.2. Bending creep

Bending tests are used to identify the value of the friction angle from the position of the neutral axis. The maximum deflection at the bottom centre of the specimen is usually a validation data [20]. In this section, a focus is made on low eccentricity values, since compression tests are sensitive to high eccentricity values, and allow much lower computation time thanks to cylindrical symmetry. Figs. 11–13 show that bending creep tests are unsensitive to low eccentricity, too. The sensitivity to dilation angle is more significant, but the effect is very weak. The sensitivity to dilation angle of deflection and out-of-plane displacement are respectively 3.3 and 0.8 μm per °. Very long tests and simulations would be required to make this sensitivity useful for identification purpose.

The relative location of the neutral-axis (Fig. 12) based on creep (CE11) or total (LE11) axial strain are very similar (Fig. 12) and the strain profile are almost linear. The axial stress (S11) profile is much more complex and do not allow a proper identification of neutral axis, but it is not an issue since these data are not reachable by experiment. Fig. 13 shows that the strain-based neutral-axis reaches a quasi-steady location after a few hundreds of seconds. The sensitivity to dilation angle of the neutral axis location is 0.19 mm per °. This result is somewhat useful for identification since it doesn't require long computation, but a way to distinguish the effects of friction angle β and dilation angle ψ is still to be found.

3.1.3. Diametral compression creep

Fig. 14 plots the out-of-plane displacement after 1 h creep in diametral compression along the horizontal axis at the surface of the specimen. It shows that displacements of about 0.05 mm are achieved after 1

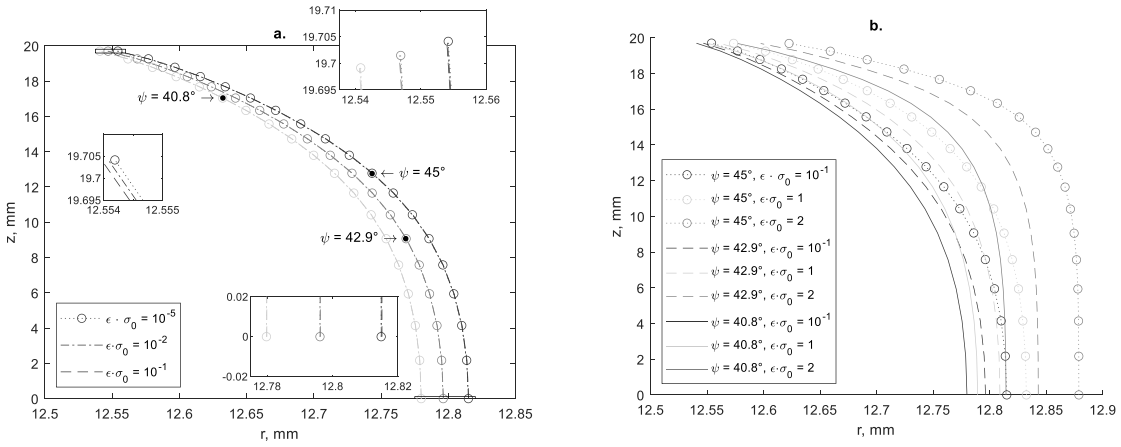

Fig. 10. Profile of the compression sample computed for several values of dilation angle ψ and eccentricity $\varepsilon \bullet \overline{\sigma}_0$ (in MPa) (a.) for low eccentricity values and (b.) for high eccentricity values.

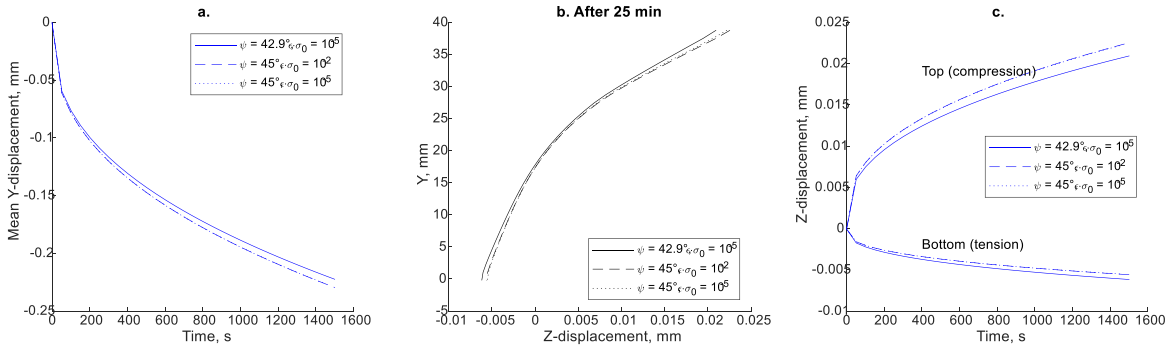

Fig. 11. (a.) maximum deflection, (b.) out-of-plane displacement after 25 min creep at 1200 °C and (c.) minimum and maximum out-of-plane displacement at the middle of the specimen, computed for several values of dilation angle ψ and eccentricity $\varepsilon \bullet \overline{\sigma}_0$ (in MPa).

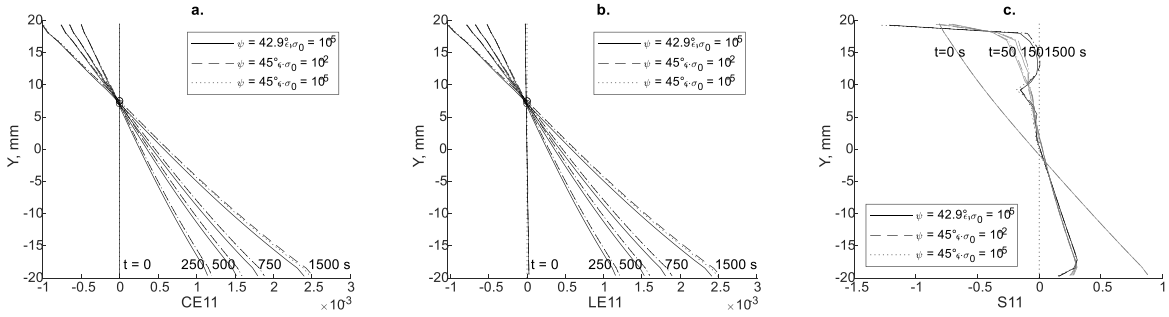

Fig. 12. (a.) creep strain CE11 (b.) total strain LE11 and (c.) stress S11, in the length-wise direction of the sample at several times and computed for several values of dilation angle ψ and eccentricity $\varepsilon \bullet \overline{\sigma}_0$ (in MPa).

h. The difference of out-of-plane displacement after 1 h with $\psi = 42.9°$ and $\psi = 45°$ is only of 3.6 μm. However, the plot of the displacement at the specimen centre as a function of time shows that the curves diverge and more significant differences are expected for longer creep times.

3.2. Experiments

3.2.1. Assessment of measurement uncertainty with natural texture of the refractory concrete at 1200 °C

The uncertainty of 3D-DIC measurements at 1200 °C is assessed by measuring the displacement of an undeformed specimen after a 1° rotation around the vertical axis. The typical physical size of a pixel is 0.018 mm. 3D-DIC was performed using VIC-3D on subsets of 73 pixels × 73 pixels with a step of 7 pixels. The rigid body motion is then removed and the measurement uncertainty is directly assimilated to the residual displacements. Fig. 15 shows the histograms of horizontal, vertical and out-of-plane displacements without any filter and with the green filter for one pair of images. Statistics of the histograms are reported in Table 3. The results evidence that the measurements are unbiased, and that the measures with the green filter are slightly more dispersed, with a d_{95} value 2.5 times higher than without the filter. Nevertheless, the values of d_{99} are of the same order of magnitude.

3.2.2. Thermal expansion

3D-DIC measurements were performed using VIC-3D while heating the cylindrical and the parallelepipedal samples from room temperature

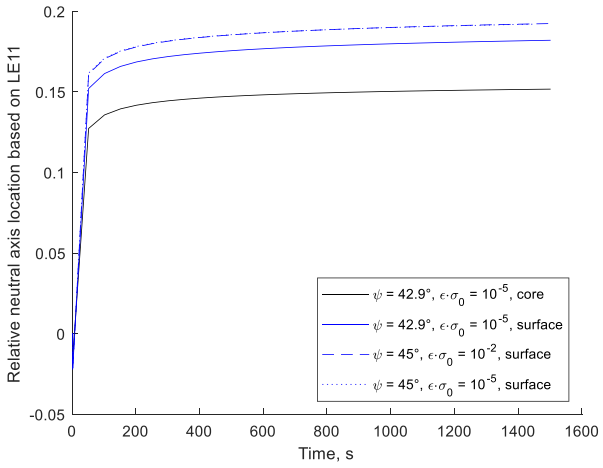

Fig. 13. Relative vertical location of the neutral axis based on LE11 $\left(\frac{y|_{LE11=0}}{h}\right)$, with the y-origin in the mid-height of the sample, at the surface and at core of the sample, as a function of time for several values of dilation angle ψ and eccentricity $\varepsilon \bullet \overline{\sigma}_0$ (in MPa).

up to 1200 °C. Images were acquired with additional light at room temperature, and without additional light at high temperature. For the cylindrical sample, an AOI of 310 pixels width and 1560 pixels height was considered, the typical physical size of a pixel is 0.021 mm, and 3D-DIC was performed on large subsets of 125 pixels × 125 pixels with a step of 20 pixels to have a smooth measure of overall thermal expansion. For the parallelepipedal sample, the typical physical size of a pixel is 0.018 mm, and 3D-DIC was performed on subsets of 73 pixels × 73 pixels with a step of 7 pixels, and the AOI was 1020 pixels wide and 910 pixels high. The strain related to thermal expansion was computed from the average slope of coordinate at high temperature plotted as a function of coordinate at room temperature. The results are reported in Fig. 16 and show that the strain is consistent in all measurements and of the order of magnitude of the dilatometric curve reported in Ref. [24] in this range of temperature.

3.2.3. Curvature of a cylindrical sample

In section 3.1.1, the effect of dilation angle and eccentricity on the compression sample profile was investigated. The present section is the experimental counterpart and focuses on the curvature analysis of a cylindrical profile along the cylinder axis direction (vertical) and in the mid-height plane (horizontal).

3D-DIC measurements were performed using VIC-3D on the same cylindrical sample at room temperature and 1200 °C. Images were acquired with additional light at room temperature, and without additional light at high temperature. An AOI of 470 pixels width and 1430 pixels height was considered, the typical physical size of a pixel is 0.021 mm, and 3D-DIC was performed on subsets of 47 pixels × 47 pixels with

Table 3
Statistics of displacement uncertainty in mm related to rigid body motion (1° rotation).

		Average (mm)	St. dev. (mm)	d_{95} (mm)	d_{99} (mm)
No filter	U	$-2.80\cdot10^{-4}$	0.0048	0.0094	0.018
	V	$-3.54\cdot10^{-12}$	0.0066	0.0070	0.016
	W	$2.92\cdot10^{-12}$	0.012	0.014	0.041
Green filter	U	$5.54\cdot10^{-6}$	0.011	0.019	0.023
	V	$-6.36\cdot10^{-13}$	0.0061	0.012	0.019
	W	$-7.34\cdot10^{-12}$	0.019	0.037	0.045

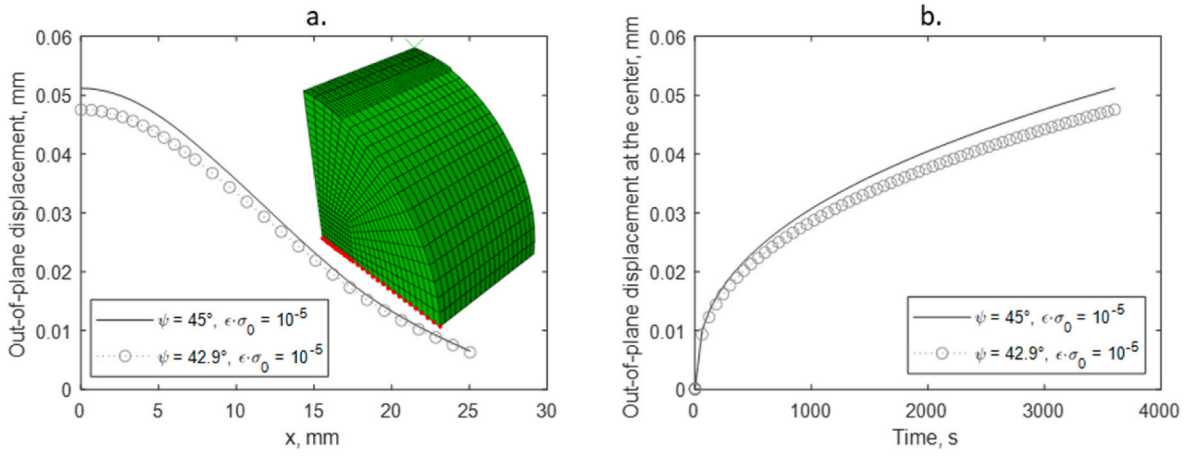

Fig. 14. Out-of-plane displacement after 1 h creep at 1200 °C in diametral compression along the horizontal axis at the surface of the specimen (a.) and out-of-plane displacement as a function of time at the centre of the specimen assuming to values of dilation angle (b.). Eccentricity $\varepsilon \bullet \overline{\sigma}_0$ in MPa.

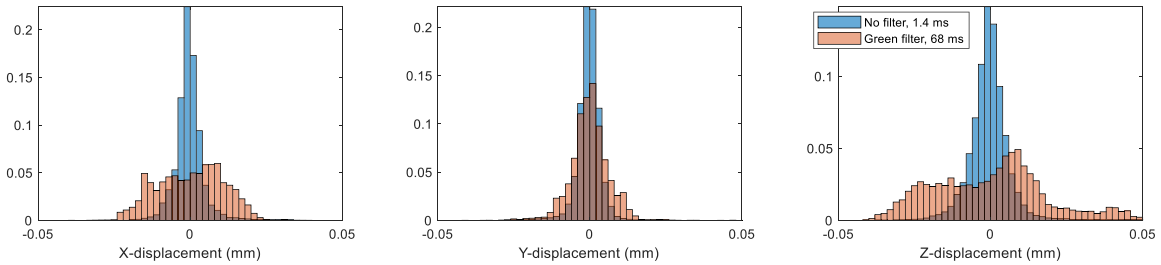

Fig. 15. Histograms of X-, Y- and Z-displacements of 1° tilted sample measured at 1200 °C after removing rigid body motion.

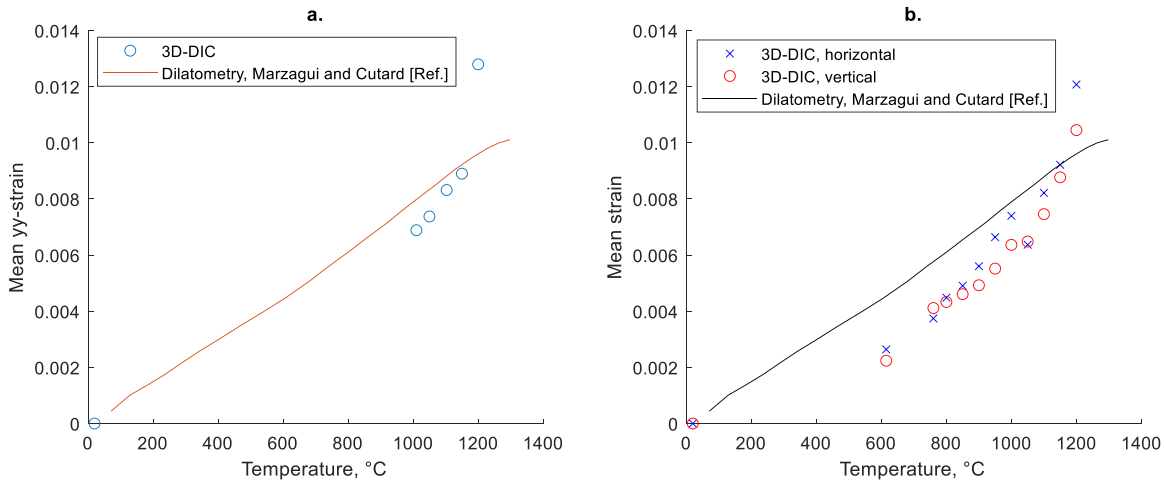

Fig. 16. Thermal expansion strain of (a.) a cylindrical sample (vertical axial strain) and (b.) of the flat surface of a parallelepipedal sample (in horizontal and vertical directions), measured by 3D-DIC from room temperature up to 1200 °C, compared to the dilatometric curve in Ref. [24] (same refractory concrete, but unreinforced by metallic fibres). A large part of the gap is related to the different thermal management and sample volume in both experiments.

a step of 7 pixels.

Fig. 17 illustrates the 3D-DIC measurement at 1200 °C, and shows the profiles extracted from the surface for curvature analysis along the X-axis (mid-height plane), Fig. 18, and along the Y-axis (vertical axis of the cylinder), Fig. 19.

The first result is that 3D-DIC is able to provide very similar results at room temperature and at 1200 °C. As expected, the profile in the mid-height plane (Fig. 18) is very close to a circle, allowing a very proper curvature identification. The nominal initial radius of the cylinder is 12.5 mm, and the radii of curvature measured after compression creep are respectively of 13.1 mm at 1200 °C and 13.0 mm at room temperature. It is noteworthy that the difference of radius is of the order of magnitude of the thermal expansion expected between room temperature and 1200 °C.

The profile extracted in the axis of the cylinder (Fig. 19) is much more rough, due to the very low curvature in this direction. However, high temperature is not the issue, since similar circular fits are provided at room temperature and 1200 °C, with average curvature radii of respectively 764 and 777 mm.

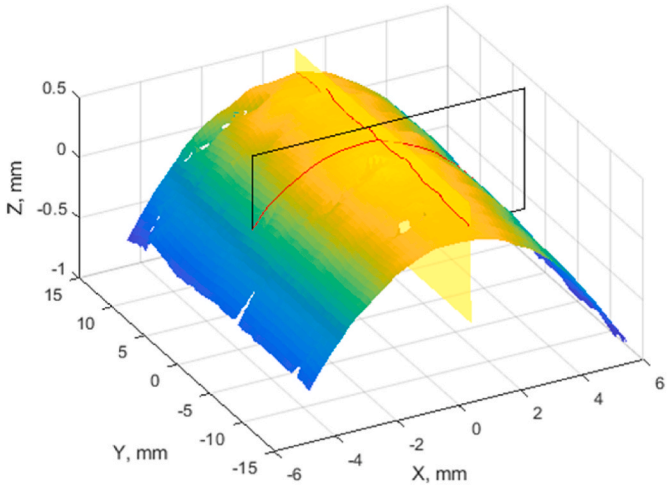

Fig. 17. Surface measured by 3D-DIC on a cylindrical sample at 1200 °C. The red lines are the profiles extracted to perform curvature analysis (Figs. 18 and 19). (For interpretation of the references to colour in this figure legend, the reader is referred to the Web version of this article.)

4. Discussion

Since the intended measurements do not require local values, but more general average data, the d_{95} value will be used in the discussion as uncertainty of displacement measurement. The results of Table 2 (converted from pixel into mm) and Table 3 are sum up in Table 4, keeping the highest absolute value among all available for U and V.

The bias is an order of magnitude lower than d_{95} and is not considered in uncertainty. Without any filter, the uncertainty related to in-plane displacement is typically below 0.01 mm with subsets of 1.3 mm and 0.03 mm with subset size of 0.5 mm. The out-of-plane measurement uncertainty is below 0.02 mm. The green filter slightly increases the uncertainty with subset size of 1.3 mm, typically below 0.02 in-plane and 0.04 out-of-plane, but decreases the in-plane uncertainty below 0.02 mm with subsets of 0.5 mm. This result can be related to the increase in MTF (Fig. 8) at high frequency discussed in section 2.4.3.

4.1. In-plane displacement

3D-DIC may be used to measure the deflection in bending tests. Such a contactless measurement will provide more reliable results than LVDT sensors because of the complex setup of the latter. The uncertainty of in-plane measurement, about 0.01 mm allows to accurately measure the deflection, whose order of magnitude is of 0.2 mm (Fig. 11.a). In section 3.1.2, the sensitivity to dilation angle of deflection was assessed to 3.3 µm per °, i.e. an order of magnitude lower than uncertainty. This measurement is therefore sensitive only to large dilation angle change.

4.2. Out-of-plane measurements

The order of magnitude of out-of-plane displacements reported in Fig. 11.b for bending creep is of 0.02 mm, which is of the level of uncertainty. Moreover, the sensitivity to dilation angle (0.8 µm per °) is much lower than uncertainty. This means that the method will not be able to provide data useful for identification. However, Fig. 11.c shows that the value increases with time and longer experiments are likely to provide data to check the relevance of the model.

Similar conclusions can be drawn about diametral compression: the order of magnitude of the out-of-plane displacement is 0.05 mm (Fig. 14. b), i.e. a few times the uncertainty level. The sensitivity to dilation angle of out-of-plane displacement is 1.7 µm per ° (section 3.1.3). These values will increase with time, and computation is faster for diametral compression than for bending creep. Diametral compression is then

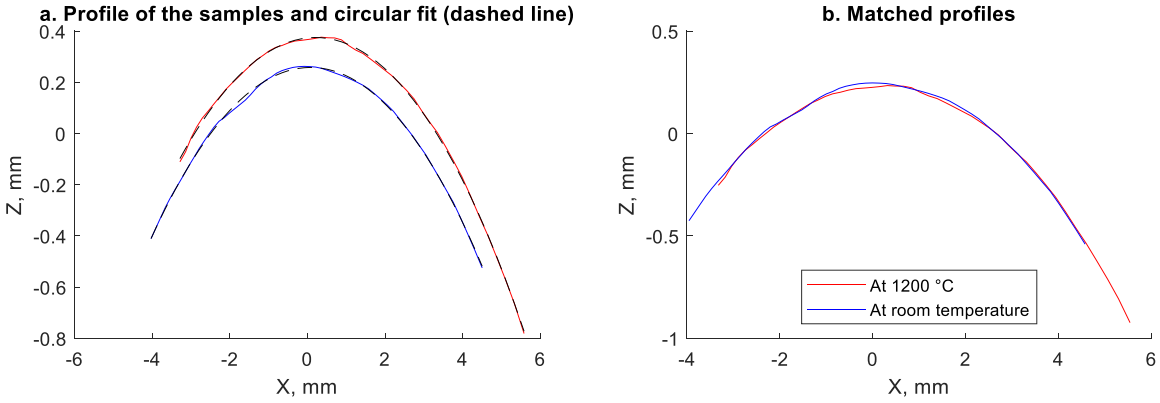

Fig. 18. Sample profiles along X-axis at 1200 °C and room temperature.

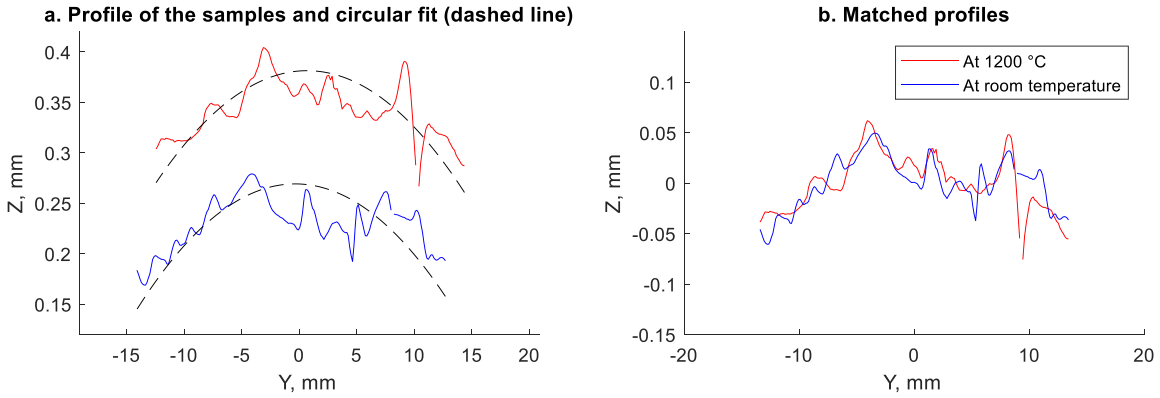

Fig. 19. Sample profiles along Y-axis at 1200 °C and room temperature.

Table 4
Displacement uncertainty at 1200 °C.

		Subset size 1.3 mm (Table 3)		Subset size 0.5 mm (Table 2)	
		Bias (mm)	d_{95} (mm)	Bias (mm)	d_{95} (mm)
No filter	U	$2.80{\cdot}10^{-4}$	0.0094	0.00220	0.0229
	V	$3.54{\cdot}10^{-12}$	0.0070	0.00185	0.0272
	W	$2.92{\cdot}10^{-12}$	0.014	–	–
Green filter	U	$5.54{\cdot}10^{-6}$	0.019	0.001372	0.0165
	V	$6.36{\cdot}10^{-13}$	0.012	0.00437	0.0198
	W	$7.34{\cdot}10^{-12}$	0.037	–	–

more suitable to perform several simulations for a rough identification, but it requires much longer experiments, of several hours, instead of 1 h for bending.

4.3. Curvature of cylindrical samples

Section 3.2.3 shows that the lower curvature radius of cylindrical samples can be extracted with a high level of confidence from the 3D-DIC measurements at 1200 °C, as well as at room temperature. This measure is more profitable than just monitoring the profile change with time to compare to numerical data. Indeed, in the experiments, the symmetry around the axis of the sample cannot be ensured and the profile can translate because of asymmetric friction for instance.

The measurement of the curvature in the vertical plane is not relevant because the roughness of the sample is large and the curvature very low. However, an extraction of the curvature in horizontal planes at several heights would be useful to compare to simulated data, as reported in Fig. 10. The uncertainty in out-of-plane displacement, about 0.02 mm and averaging by identification of the radius of curvature allows expecting experimental data accurate enough for rough identification purpose. The sensitivity to dilation angle of the mid-plane radius is of 8 µm per ° in the case of low eccentricity (Fig. 10.a). In the case of high eccentricity, either dilation angle (sensitivity 0.01 mm per °) or eccentricity (sensitivity 0.025 mm.MPa^{-1}) could be assessed.

4.4. Strain measurement

A careful analysis of strain uncertainty has not been performed yet, but in view of the thermal expansion measurements reported in Fig. 16, principal strain levels as low as 10^{-3} are likely to be measured by averaging over a large AOI.

This uncertainty is low enough for measuring the axial strain in compression creep tests, whose order of magnitude (Fig. 9) is of 0.015. This will avoid tedious measurement of the machine stiffness at high temperature or complex LVDT setup. However, the uncertainty is not low enough to allow an identification of dilation angle and eccentricity.

Strain levels from -10^{-3} up to $2.5 \bullet 10^{-3}$ are reported in Fig. 13 after 25 min of bending creep. These values are compatible with an extraction of neutral axis location from 3D-DIC measurement by averaging along horizontal lines between the upper span, and even more accurate results are expected for longer creep experiments.

The sensitivity to dilation angle and eccentricity is very low and confirms that monitoring the neutral-axis location in bending creep experiments is an excellent way to identify the friction angle. Unfortunately, this identification requires 3D simulations of high computational cost. Indeed, in Ref. [20], using plane-strain simulations of bending tests and 3D-DIC at room temperature after interrupted tests, a friction angle of 42.9° was identified assuming associated flow. In the present paper,

using 3D simulation shows that the neutral-axis defined as the iso-surface LE11=0 is not constant across the sample (cf. Fig. 13). The relative neutral axis location at the surface, which in turn corresponds to the experimental one, is found to be of 0.18, whereas the experimental value is 0.28 [8]. This shows that 2D simulations are not relevant for friction angle identification from DIC surface measurements.

5. Conclusion

In this paper, it was investigated how 3D-DIC at high temperature would contribute to Drucker-Prager creep model calibration by providing out-of-plane displacement fields, which are of importance to understand the dilatant behaviour of the material.

It has been shown that the natural texture of the material constituted a relevant pattern for DIC, despite the loss of contrast at high temperature. The main limitation is related to the size of the aggregates, which requires to choose the subset size accordingly. Using a green filter is a lead to be further explored to allow lower subset size. Indeed, it results in a higher amount of light in the chromatism correction range, which seems to provide a better contrast, specifically at high frequency.

The heat haze turns out to be the main limitation for more accurate measurement, in particular because of its different effect on both cameras. However, the level of uncertainty of displacement measurement was found to be of 0.01 mm in-plane and 0.02 mm out-of-plane.

The numerical analysis has shown that 3D simulations are required to calibrate the friction angle from neutral axis location in bending creep experiment, since the 2D simulations are not representative of the surface strain field, which is the reference experimental data.

A comparison of measurement uncertainty and numerical sensitivity analysis shows that 3D-DIC at high temperature is a promising way to acquire experimental data of importance for model calibration:

- The deflection in bending creep experiments can be monitored with a sufficient level of uncertainty, but is not sensitive enough to dilation angle to consider accurate identification.
- The out-of-plane displacement can be measured with a sufficient level of uncertainty to (i) bring confirmation of the dilatant behaviour of the material in bending and diametral compression creep tests, and (ii) to provide curvatures of cylindrical samples allowing a rough identification of dilation angle or eccentricity.
- 3D-DIC provides a contactless measure of axial strain in compression creep tests.
- The neutral axis location can be monitored with a sufficient level of uncertainty and is almost insensitive to dilation angle and eccentricity, which confirms its relevance for friction angle identification.

These conclusions pave the way for a more exhaustive calibration method using high temperature 3D-DIC.

Declaration of competing interest

The authors declare that they have no known competing financial interests or personal relationships that could have appeared to influence the work reported in this paper.

Acknowledgement

The authors gratefully acknowledge the contributions of Didier Adé, Rémi Gilblas, Thomas Papaïx and Fabrice Rossi to the experimental results.

References

[1] A.A. Wereszczak, M.K. Ferber, T.P. Kirkland, A.S. Barnes, E.L. Frome, M.N. Menon, Asymmetric tensile and compressive creep deformation of hot-isostatically-pressed Y_2O_3-doped -Si_3N_4, J. Eur. Ceram. Soc. 19 (1999) 227–237, https://doi.org/10.1016/S0955-2219(98)00184-8.

[2] R.S. Kottada, A.H. Chokshi, The high temperature tensile and compressive deformation characteristics of magnesia doped alumina, Acta Mater. 48 (2000) 3905–3915.

[3] Massard Ludovic Massard, Kamel Madi, Michel Boussuge, Samuel Forest, Edwige Yeugo-Fogaing, Marc Huger, Christian Gault, High Temperature Mechanical Behavior of Fused Cast Refractories, 43rd Annual Conference of Metallurgists of CIM, August 2004, pp. 631–644. Hamilton, Canada, 22-25.

[4] Lucas Teixeira, Soheil Samadi, Jean Gillibert, Shengli Jin, Thomas Sayet, Dietmar Gruber, Eric Blond, Experimental investigation of the tension and compression creep behavior of alumina-spinel refractories at high temperatures, Ceramics 3 (2020) 372–383, https://doi.org/10.3390/ceramics3030033.

[5] S.I. Warshaw, F.H. Norton, Deformation behavior of polycrystalline aluminum oxide, J. Am. Ceram. Soc. 45 (1962) 479–486.

[6] A.R. Rosenfield, D.K. Shetty, W.H. Duckworth, Estimating tensile creep data from flexure data, J. Am. Ceram. Soc. 69 (1986) 108–109.

[7] E. Blond, N. Schmitt, F. Hild, Ph. Blumenfeld, J. Poirier, Modelling of high temperature asymmetric creep behavior of ceramics, J. Eur. Ceram. Soc. 25 (2005) 1819–1827.

[8] G. Dusserre, F. Nazaret, L. Robert, T. Cutard, Applicability of image correlation techniques to characterise asymmetric refractory creep during bending tests, J. Eur. Ceram. Soc. 33 (2013) 221–231.

[9] P. Leplay, O. Lafforgue, F. Hild, Analysis of asymmetrical creep of a ceramic at 1350°C by digital image correlation, J. Am. Ceram. Soc. 98 (2015) 2240–2247, https://doi.org/10.1111/jace.13601.

[10] Lucas Breder Teixeira, Numerical Modeling and Experimental Characterization of the Asymmetric Creep Behavior of Refractory Materials, PhD Thesis, Université d'Orléans, France, 2022.

[11] T.J. Chuang, Estimation of power-law creep parameters from bend test data, J. Mater. Sci. 21 (1986) 165–175.

[12] S.M. Wiederhorn, L. Chuck, E.R. Fuller Jr., N.J. Tighe, in: R.E. Tressler, G. L. Messing, C.G. Pantano, R.E. Newnhan (Eds.), Creep Rupture of Siliconized Silicon Carbide, Material Science Research, Tailoring Multiphase and Composite Ceramics, vol. 20, Plenum Press, New York, 1986, pp. 755–773.

[13] C.F. Chen, T.J. Chuang, Improved analysis for flexural creep with application to SiAlON ceramics, J. Am. Ceram. Soc. 73 (1990) 2366–2373.

[14] M.W. Bird, R.P. Aune, F. Yu, P.F. Becher, K.W. White, Creep behavior of a zirconium diboride–silicon carbide composite, J. Eur. Ceram. Soc. 33 (2013) 2407–2420, https://doi.org/10.1016/j.jeurceramsoc.2013.03.022.

[15] Stefan Schachner, Shengli Jin, Dietmar Gruber, Harald Harmuth, Creep characterization and modelling of ordinary refractory ceramics under combined compression and shear loading conditions, Ceram. Int. 48 (Issue 15) (2022) 21101–21109, https://doi.org/10.1016/j.ceramint.2022.03.184. ISSN 0272-8842.

[16] Jacques Poirier, Eric Blond, Emmanuel de Bilbao, Rudy Michel, Coulon Antoine, Jean Gillibert, Michel Boussuge, Yang Zhang, David Ryckelynk, Gilles Dusserre, Thierry Cutard, Leplay Paul, New advances in the laboratory characterization of refractories: testing and modelling, Metall. Res. Technol. 114 (2017) 610.

[17] Anthony Delmas, Yannick Le Maoult, Jean-Marie Buchlin, Thierry Sentenac, Jean-José Orteu, et al., Shape distortions induced by convective effect on hot object in visible, near infrared and infrared bands, Exp. Fluid 54 (4) (2013) 1452, https://doi.org/10.1007/s00348-012-1452-8.

[18] Linh Phuong Luong, Rébecca Bonnaire, Jean-Noël Périé, Quentin Sirvin, Luc Penazzi, et al., Speckle pattern creation methods for two-dimensional digital image correlation strain measurements applied to mechanical tensile tests up to 700°C, Strain 57 (5) (2021) 1, https://doi.org/10.1111/str.12388, 19/e12388.

[19] B. Pan, D. Wu, Z. Wang, Y. Xia, High-temperature digital image correlation method for full-field deformation measurement at 1200 °C, Meas. Sci. Technol. 22 (1) (2011), 015701, https://doi.org/10.1088/0957-0233/22/1/015701.

[20] Gilles Dusserre, Olivier Valentin, Fabien Nazaret, Thierry Cutard, Experimental and numerical investigation of the asymmetric primary creep of a fibre reinforced refractory concrete at 1200 degrees C, J. Eur. Ceram. Soc. 36 (10) (2016) 2627–2639, https://doi.org/10.1016/j.jeurceramsoc.2016.03.007.

[21] Stefan Schachner, Shengli Jin, Dietmar Gruber, Harald Harmuth, A method to characterize asymmetrical three-stage creep of ordinary refractory ceramics and its application for numerical modelling, J. Eur. Ceram. Soc. 39 (Issue 14) (2019) 4384–4393, https://doi.org/10.1016/j.jeurceramsoc.2019.06.010. ISSN 0955-2219.

[22] M.A. Sutton, J.H. Yan, V. Tiwari, H.W. Schreier, J.J. Orteu, The effect of out-of-plane motion on 2D and 3D digital image correlation measurements, Opt Laser. Eng. 46 (2008) 746–757.

[23] J.-P. Chambard, S. Jaminion, M. Tazeroualti, C. Galerne et, F. Hild, 3D displacement field measurement by digital image correlation - metrological study and application to composite structures, in: Comptes Rendus des JNC 16 – Toulouse, 2009 (In French).

[24] H. Marzagui, T. Cutard, Characterisation of microstructural evolutions in refractory castables by in situ high temperature ESEM, J. Mater. Process. Technol. 155–156 (2004) 1474–1481, https://doi.org/10.1016/j.jmatprotec.2004.04.365.

[25] F. Nazaret, H. Marzagui, T. Cutard, Influence of the mechanical behaviour specificities of damaged refractory castables on the Young's modulus determination, J. Eur. Ceram. Soc. 26 (2006) 1429–1438, https://doi.org/10.1016/j.jeurceramsoc.2005.03.231.

[26] Abaqus, Documentation. Providence, RI, USA, Dassault Systèmes Simulia Corp, 2018.

[27] Thierry Cutard, Nicolas Donval, Aurélien Mazzoni, Claire Michel, Fabien Nazaret, Thermomechanical characterization of monolithic refractory castables Advances in Science and Technology, Trans Tech Publications 70 (2010) 37–46. https://doi.org/10.4028/www.scientific.net/AST.70.37.

[28] Pike Technical Manual, V5.2.4, Allied Vision Technologies GmbH, 2018-Dec-14.
[29] F. Sigernes, M. Dyrland, N. Peters, D. Lorentzen, T. Svenøe, K. Heia, S. Chernouss, C. Deehr, M. Kosch, The absolute sensitivity of digital colour cameras, Opt Express 17 (22) (2009) 20211–20220, https://doi.org/10.1364/OE.17.020211.
[30] https://www.dpreview.com/forums/post/60990312 last accessed 19/05/2023.
[31] https://www.lensrentals.com/blog/2018/03/a-geek-of-many-colors-adventures-in-spectrometry/ last accessed 19/05/2023.
[32] https://www.graphics.cornell.edu/online/measurements/filter-spectra/index.html last accessed 19/05/2023.
[33] Bing Pan, Zixing Lu, Huimin Xie, Mean intensity gradient: an effective global parameter for quality assessment of the speckle patterns used in digital image correlation, Opt Laser. Eng. 48 (2010) 469–477.
[34] E. Jones, P. Reu, Distortion of digital image correlation (DIC) displacements and strains from heat waves, Exp. Mech. 58 (2018) 1133–1156.
[35] Karel. Zuiderveld, Contrast limited adaptive histograph equalization, Graphic Gems IV. San Diego: Academic Press Professional (1994) 474–485.